Supporting Information

π-4f charge-transfer emission in a trivalent europium complex

Yuichi Kitagawa[1,2]*, Toranosuke Tomikawa[3], Kota Aikawa[3], Shiori Miyazaki[4], Tomoko Akama[2], Masato Kobayashi[2,5], Mengfei Wang[2], Sunao Shoji[6], Koji Fushimi[1], Kiyoshi Miyata[4], Yuichi Hirai[7], Takayuki Nakanishi[7], Ken Onda[4], Tetsuya Taketsugu[2,5], and Yasuchika Hasegawa[1,2]*

[1]Faculty of Engineering, Hokkaido University, Kita 13, Nishi 8, Kita-ku, Sapporo, Hokkaido 060–8628, Japan.

[2]Institute for Chemical Reaction Design and Discovery (WPI-ICReDD), Hokkaido University, Kita 21, Nishi 10, Kita-ku Sapporo, Hokkaido 001-0021, Japan.

[3]Graduate School of Chemical Sciences and Engineering, Hokkaido University, Kita 13, Nishi 8, Sapporo, Hokkaido 060-8628, Japan.

[4]Department of Chemistry, Kyushu University, 744 Motooka, Nishi, Fukuoka 829-0395, Japan.

[5]Faculty of Science, Hokkaido University, Kita 10, Nishi 8, Kita-ku, Sapporo, Hokkaido 060-0810 Japan.

[6]Department of Engineering, Nara Women's University, Kitauoya-Nishimachi, Nara 630-8506, Japan.

[7]National Institute for Materials Science, 1-1 Namiki, Tsukuba, Ibaraki 305-0044, Japan.

S1. Chemical structures

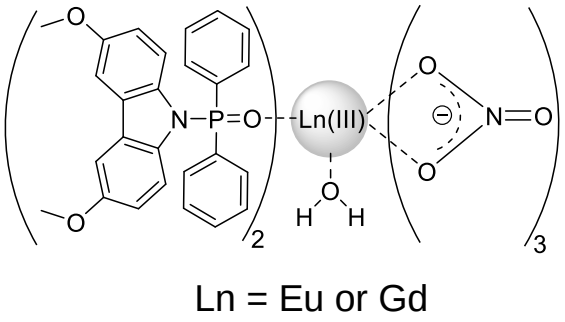

Figure S1. Chemical structures of nine-coordinated Eu(III) (**Eu-MCPO-H_2O**) and Gd(III) (**Gd-MCPO-H_2O**) complexes.

S2. Experimental section

Computational details: All quantum chemical calculations were performed using the density functional theory (DFT) using the Gaussian 16 package.[S1] The ground state geometry optimization was carried out using DFT with the B3LYP-D3 functional,[S2-S4] and the investigation into excited states utilized time-dependent DFT (TD-DFT) with the long-range corrected (LC) BLYP functional.[S5-S7] The Stuttgart RECP basis set[S8] was adopted for Eu atoms, and for the remaining atoms, including C, H, N, O, and P, the cc-pVDZ basis set[S9-S10] was used. The solvent effect was considered using the Polarizable Continuum Model (PCM) method.[S11] GaussSumS17 was employed to assess atomic orbital contributions to the molecular orbitals (MOs).

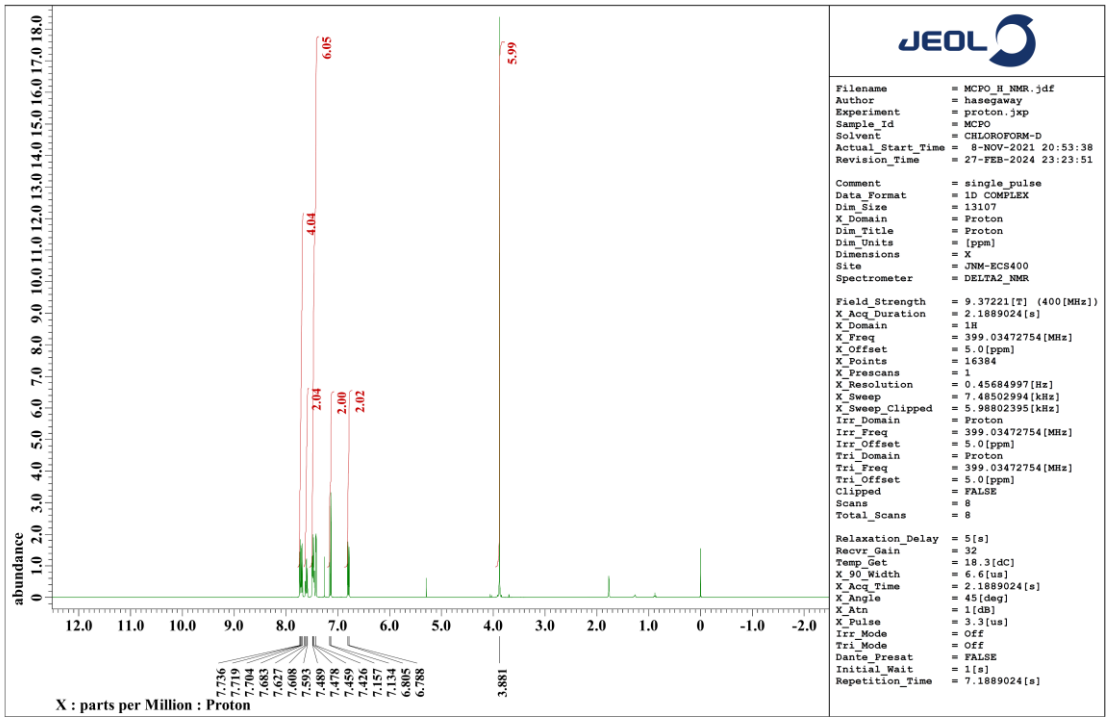

Figure S2. ^{1}H NMR chart of MCPO

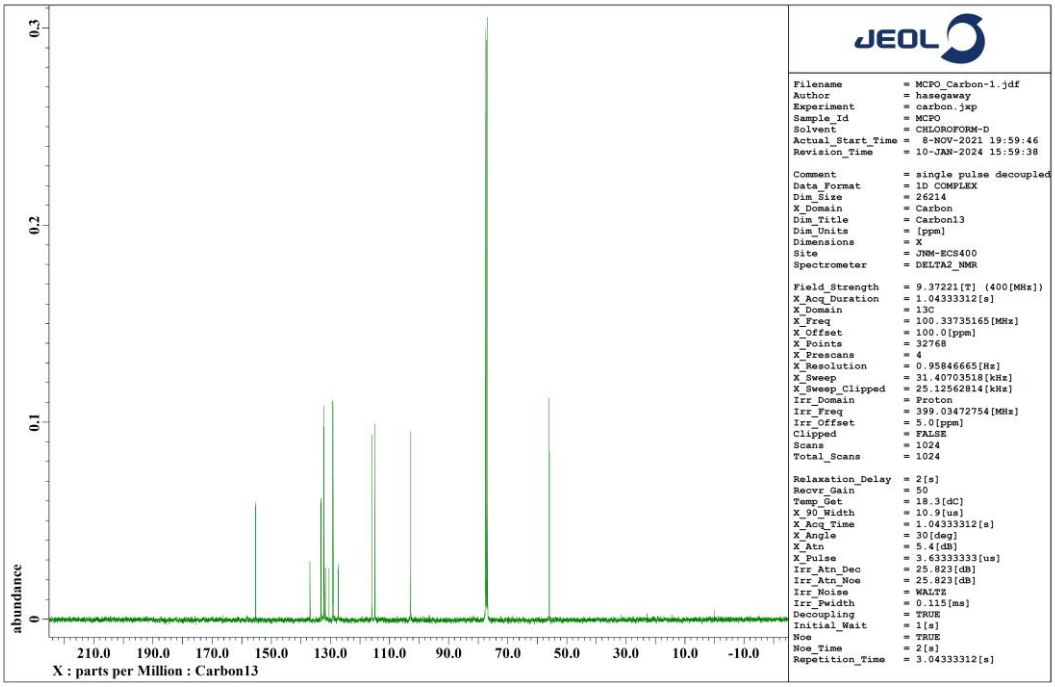

Figure S3. ^{13}C NMR chart of MCPO

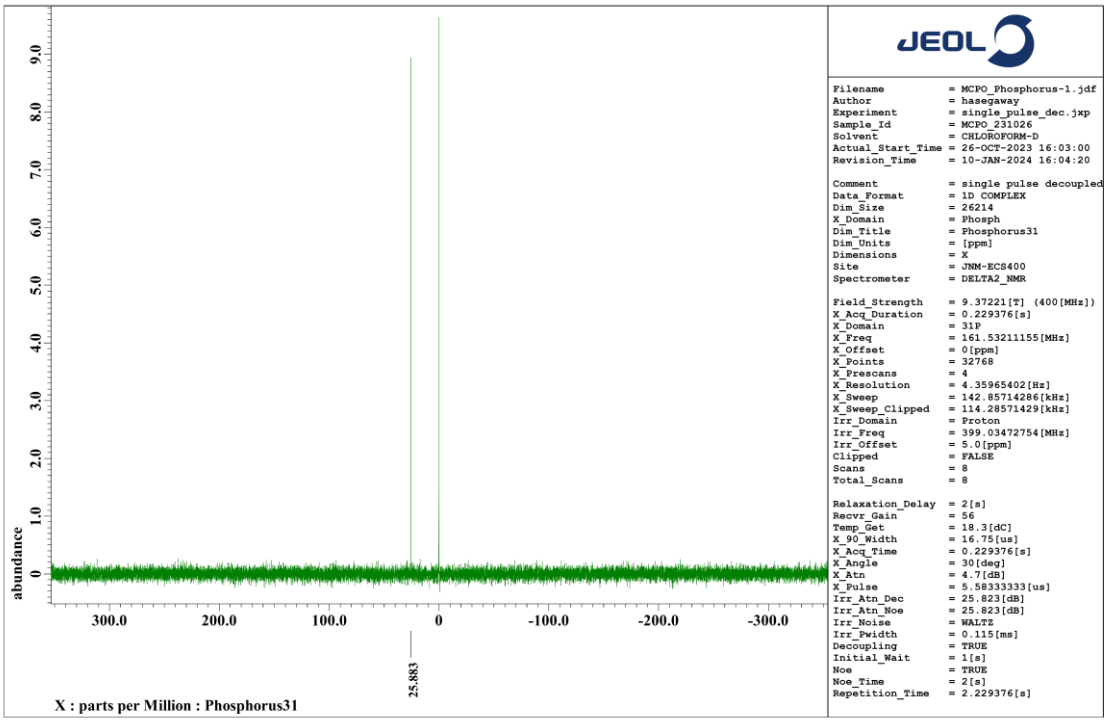

Figure S4. ^{31}P NMR chart of MCPO

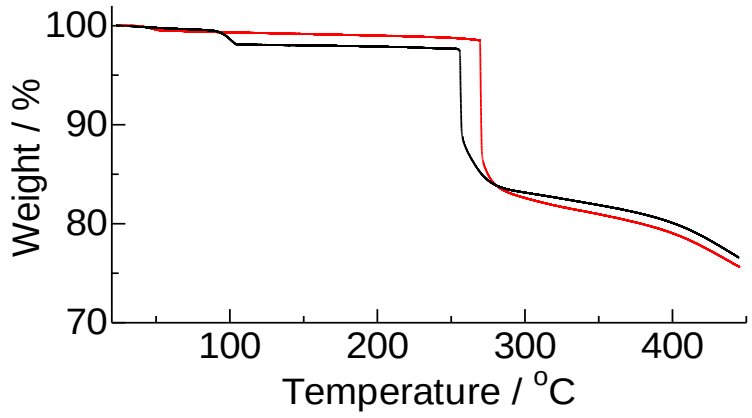

Figure S5. TG-DTA profiles of **Eu-MCPO-H_2O** (black line) and **Eu-MCPO** (red line).

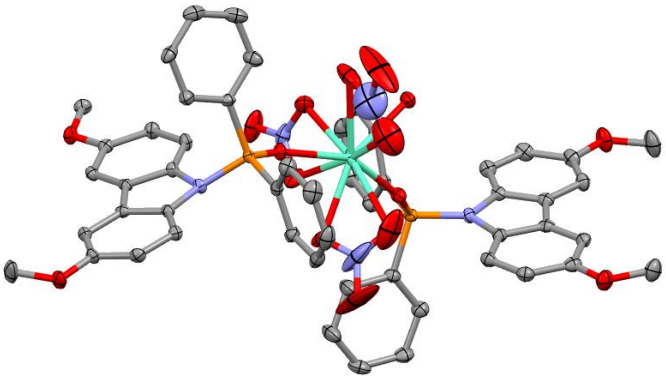

Figure S6. ORTEP drawings (ellipsoids set at 50 % probability) of **Eu-MCPO-H$_2$O**. Gray spheres represent carbon; red spheres, oxygen; purple spheres, nitrogen; orange spheres, phosphorus; and green spheres, europium.

Table S1. Crystallographic data for **Eu-MCPO-H$_2$O**

	Eu-MCPO-H$_2$O
Chemical formula	$C_{52}H_{46}EuN_5O_{16}P_2$
Formula weight	1210.84
Crystal system	Triclinic
Space group	*P-1*
a /Å	9.7632(4)
b /Å	12.0671(4)
c /Å	22.2933(9)
α /deg.	98.853(3)
β /deg.	94.890(3)
γ /deg.	102.897(3)
Volume /Å^3	2510.12(17)
Z	2
Temperature / K	1.602
d_{calc} / g cm^{-3}	−150
R_1	0.0411
wR_2	0.1048

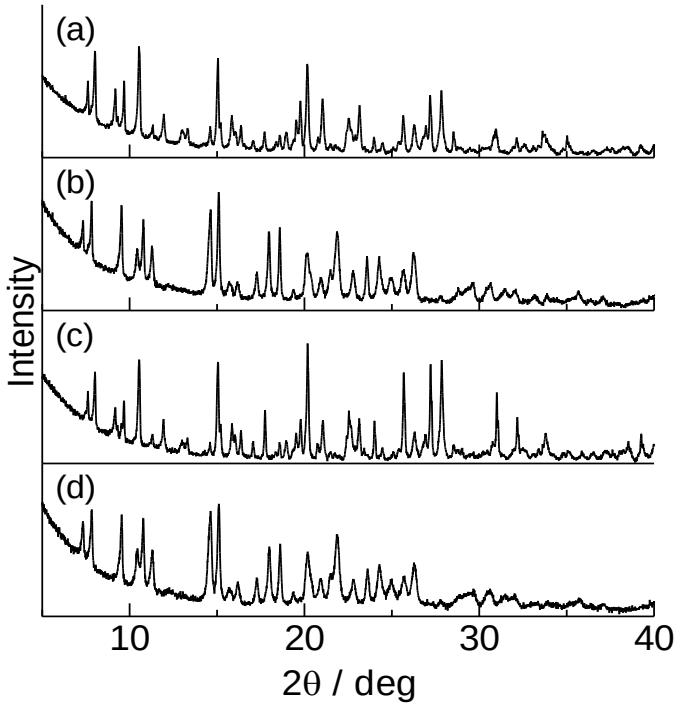

Figure S7. PXRD patterns of (a) **Eu-MCPO-H_2O**, (b) **Eu-MCPO**, (c) **Gd-MCPO-H_2O**, (d) **Gd-MCPO**

S3. Quantum chemical calculation and additional photophysical measurements

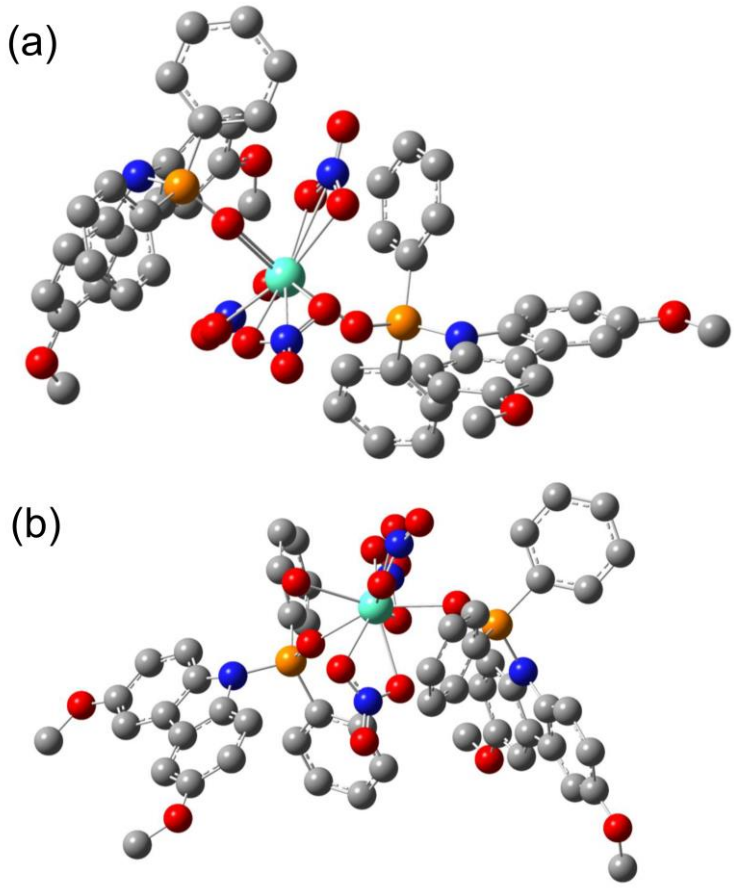

Figure S8. Optimized structure of (a) **Eu-MCPO** [average Eu−O (NO_3): 2.474 Å, average Eu–O (MCPO): 2.321 Å] and (b) **Eu-MCPO-H_2O** [average Eu−O (NO_3): 2.482 Å, average Eu–O (MCPO): 2.386 Å] in the ground state obtained by DFT calculations with vacuum condition. Gray spheres represent carbon; red spheres, oxygen; blue spheres, nitrogen; orange spheres, phosphorus; and green spheres, europium.

Table S2. Electronic transition properties in ground state of **Eu-MCPO** obtained by TDDFT calculation using the optimized structure (Figure S8).

Ex	λ/nm	f / -	Main contribution		Assignment
7	501	0.0000	290A→296A	0.45300	$\pi_{(MCPO)}$-
			284B→289B	–0.44198	$\pi^*_{(MCPO/NO3)}$
8	491	0.0000	288A→295A	0.45911	$\pi_{(MCPO)}$-
			282B→288B	–0.45833	$\pi^*_{(MCPO)}$
9	419	0.0019	290A→292A	0.65816	$\pi_{(MCPO)}$-4f
			289A→292A	0.63347	
10	417	0.0000	278B→287B	0.29122	$\pi_{(MCPO)}$-
			284B→294A	–0.28775	$\pi^*_{(MCPO)}$
			284A→305A	0.27570	
			285A→305A	0.27515	
			279B→299B	–0.26416	
			278B→299B	–0.25636	
11	414	0.0000	282A→293A	–0.34534	$\pi_{(MCPO)}$-
			276B→286B	0.34529	$\pi^*_{(MCPO)}$
			277B→296B	–0.27442	
12	411	0.0000	280A→301A	0.39328	$\pi_{(MCPO)}$-
			272B→287B	0.36658	$\pi^*_{(MCPO)}$
			278A→294A	–0.36432	
			274B→295B	–0.32955	
			274B→293B	–0.25671	
13	411	0.0000	275B→294B	–0.33412	$\pi_{(MCPO)}$-
			282A→297A	0.32890	$\pi^*_{(MCPO)}$
			281A→300A	0.30253	
			276B→290B	–0.26360	
14	392	0.0000	289A→292A	0.71210	$\pi_{(MCPO)}$-4f
			290A→292A	–0.56611	

Table S3. Atomic orbital contribution to MOs appearing in the main configuration of the lowest π-4f charge transfer excited state of **Eu-MCPO** using the optimized structure (9th excited state in Table S2). There is very small mixing of the π orbitals of MCPO and the 4f orbital of Eu.

MO	4f	MCPO-1	MCPO-2	NO_3
289A	0.00055	0.00101	0.99311	0.00421
290A	0.00018	0.00028	0.99396	0.00541
292A	0.95262	0.00402	0.00436	0.03611

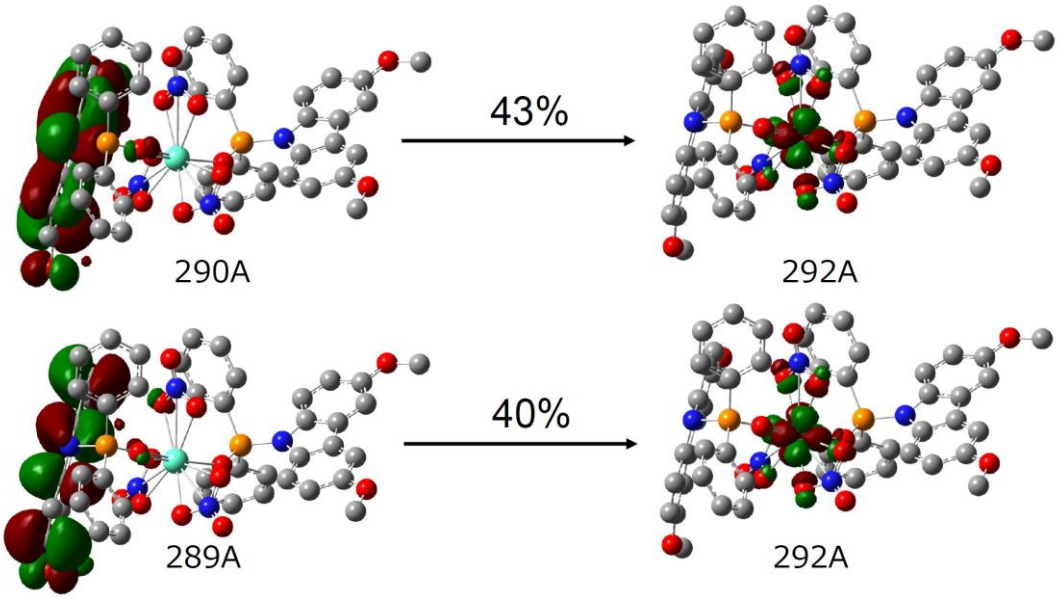

Figure S9. Transition orbital analysis of the lowest π-4f CT excited state of **Eu-MCPO** using the optimized structure (9th excited state in Table S2).

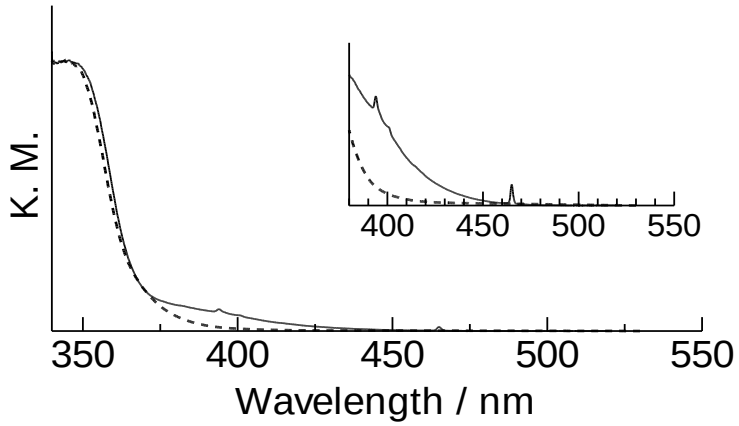

Figure S10. Diffuse reflectance spectra of **Eu-MCPO-H_2O** (black solid line) and **Gd-MCPO-H_2O** (black broken line).

Table S4. Electronic transition properties in the ground state of **Eu-MCPO-H_2O** obtained by TDDFT calculations using (a) the crystal structure (Figure S6) and (b) the optimized structure (Figure S8(b)).

(a)

Ex	λ/nm	f / -	Main contribution		Assignment
7	510	0.0000	288A→305A	0.37781	$\pi_{(MCPO\&NO3)}$-$\pi^*_{(MCPO\&NO3)}$
			282B→298B	–0.35019	
8	464	0.0000	295A→302A	0.30516	$\pi_{(MCPO)}$-$\pi^*_{(MCPO)}$
			289B→295B	–0.30325	
			289B→293B	–0.27940	
			295A→300A	0.27797	
9	462	0.0000	293A→299A	0.47485	$\pi_{(MCPO)}$-$\pi^*_{(MCPO)}$
			287B→292B	–0.47462	
10	440	0.0000	291A→305A	0.48578	$n_{(NO3)}$-$\pi^*_{(MCPO\&NO3)}$
			285B→298B	–0.44973	
			291A→304A	0.33925	
			285B→297B	–0.32301	
11	432	0.0010	291A→297A	0.85038	$n_{(NO3)}$-4f
			271A→297A	–0.32844	
12	396	0.0000	278B→295B	0.30626	$\pi_{(MCPO)}$-$\pi^*_{(MCPO)}$
			284A→302A	–0.30350	
13	395	0.0000	278A→298A	0.42064	$\pi_{(MCPO)}$-$\pi^*_{(MCPO)}$
			272B→291B	–0.41800	
14	395	0.0094	283A→297A	0.82692	$n_{(NO3)}$-4f
15	389	0.0080	280A→297A	0.68227	$n_{(NO3)}$&$\pi_{(MCPO)}$-4f
			281A→297A	0.45394	
16	389	0.0000	282A→301A	0.42235	$\pi_{(MCPO)}$-$\pi^*_{(MCPO)}$
			276B→294B	–0.40204	
			279B→301B	–0.40085	
			285A→307A	–0.40064	
17	388	0.0000	283B→304B	0.37198	$\pi_{(MCPO\&NO3)}$-$\pi^*_{(MCPO(\&NO3))}$
			289A→310A	0.34732	
18	374	0.0000	291A→305A	0.49707	n-$\pi^*_{(MCPO\&NO3)}$
			285B→298B	0.45840	
19	373	0.0000	290B→293B	0.36972	$\pi_{(MCPO)}$-$\pi^*_{(MCPO)}$
			296A→300A	–0.36831	
			292A→314A	0.28553	
			286B→313B	–0.27802	
			296A→302A	–0.27318	
20	365	0.0005	288A→297A	0.68684	$\pi_{(MCPO\&NO3)}$-4f
			289A→297A	0.42195	
21	360	0.0000	288B→292B	0.45393	$\pi_{(MCPO)}$-$\pi^*_{(MCPO)}$
			294A→299A	–0.45387	
22	351	0.0002	296A→297A	0.94852	$\pi_{(MCPO)}$-4f

(b)

Ex	λ/nm	f / -	Main contribution		Assignment
7	493	0.0000	294A→301A 288B→294B	0.40227 –0.39842	$\pi_{(MCPO)}$-$\pi^*_{(MCPO)}$
8	493	0.0000	287B→292B 293A→299A	0.41522 –0.41499	$\pi_{(MCPO)}$-$\pi^*_{(MCPO)}$
9	416	0.0000	290A→310A 284B→304B 289A→300A 283B→293B	0.40290 –0.40150 0.32688 –0.32322	$\pi_{(MCPO)}$-$\pi^*_{(MCPO)}$
10	413	0.0000	280B→299B 286A→305A 277B→291B 283A→298A 283A→299A 277B→292B	–0.35208 0.34557 –0.29061 0.28906 –0.26018 0.26012	$\pi_{(MCPO)}$-$\pi^*_{(MCPO)}$
11	411	0.0000	284A→300A 284A→303A 278B→293B 278B→296B 281B→300B	–0.32316 0.30423 0.31969 –0.30061 –0.33739	$\pi_{(MCPO)}$-$\pi^*_{(MCPO)}$
12	410	0.0000	279B→295B 285A→302A	–0.35548 –0.35754	$\pi_{(MCPO)}$-$\pi^*_{(MCPO)}$
13	379	0.0000	296A→301A 296A→315A 290B→294B	0.37264 0.27748 –0.36880	$\pi_{(MCPO)}$-$\pi^*_{(MCPO)}$
14	369	0.0000	291A→311A 295A→298A 285B→306B 289B→291B	0.29128 –0.26786 –0.27611 0.26757	$\pi_{(MCPO)}$-$\pi^*_{(MCPO)}$
15	368	0.0077	279A→297A 281A→297A 282A→297A	–0.48263 0.48876 0.58075	$n_{(NO3)}$&$\pi_{(MCPO)}$-4f
16	358	0.0026	279A→297A 282A→297A 296A→297A	–0.54273 –0.45014 0.57932	$\pi_{(MCPO)}$&$n_{(NO3)}$-4f
17	355	0.0012	279A→297A 296A→297A	0.45459 0.75266	$\pi_{(MCPO)}$(&$n_{(NO3)}$)-4f

Table S5. Atomic orbital contribution to MOs appearing in the main configuration of the first and second lowest π-4f CT excited states of **Eu-MCPO-H_2O** using the crystal structure (15th and 22nd excited state in Table S4(a)). There is very small mixing of the π orbitals of MCPO and the 4f orbital of Eu.

MO	4f	MCPO-1	MCPO-2	NO_3
280A	0.00697	0.33658	0.04773	0.59187
281A	0.00309	0.66503	0.03255	0.29097
296A	0.00002	0.99967	0.00001	0.00036
297A	0.95422	0.00261	0.00301	0.03957

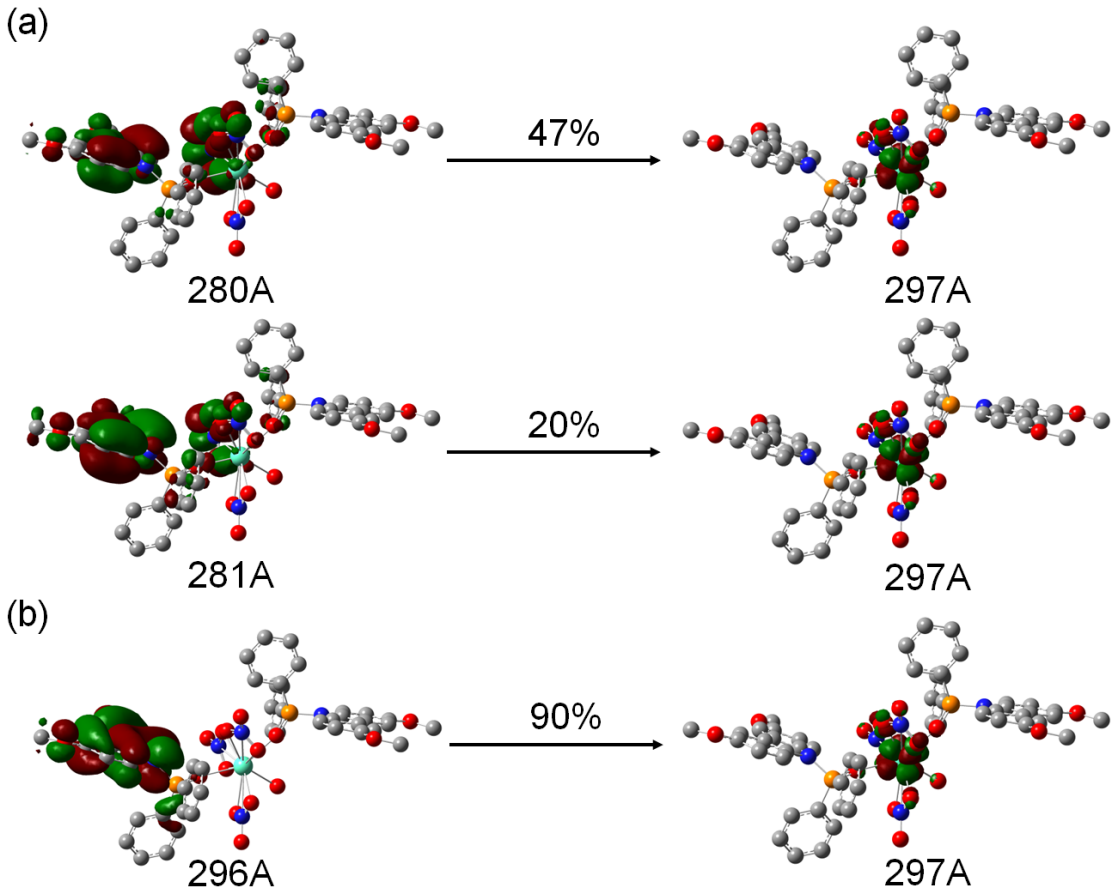

Figure S11. Transition orbital analysis of the (a) first and (b) second lowest π-4f CT excited states of **Eu-MCPO-H_2O** using the crystal structure (15th and 22nd excited state in Table S4(a)).

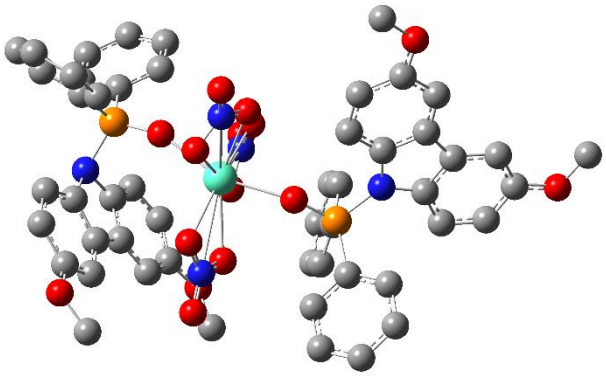

Figure S12. Optimized structure of **Eu-MCPO** in THF solvent [average Eu-O (NO3): 2.491 Å, average Eu-O (MCPO): 2.322 Å] in the ground state obtained by DFT calculations with PCM method.

Table S6. Electronic transition properties in ground state of **Eu-MCPO** in THF solvent obtained by TDDFT calculation using optimized structure (Figure S12).

Ex	λ/nm	f / -	Main contribution		Assignment
7	499	0.0000	290A→296A	0.32225	$\pi_{(MCPO)}$-
			289A→296A	–0.31225	$\pi^*_{(MCPO/NO3)}$
			283B→289B	0.30689	
			284B→289B	–0.31491	
8	490	0.0000	286A→295A	–0.29431	$\pi_{(MCPO)}$-
			288A→295A	0.44289	$\pi^*_{(MCPO)}$
			282B→288B	–0.43968	
9	445	0.0013	290A→292A	0.96338	$\pi_{(MCPO)}$-4f
10	415	0.0000	284A→294A	–0.25978	$\pi_{(MCPO)}$-
			284A→305A	–0.30418	$\pi^*_{(MCPO)}$
			285A→294A	0.24852	
			278B→287B	0.26355	
			278B→299B	0.29712	
			279B→287B	–0.24862	
11	414	0.0003	289A→292A	0.94364	$\pi_{(MCPO)}$-4f
12	413	0.0000	281A→304A	–0.24569	$\pi_{(MCPO)}$-
			282A→302A	–0.25950	$\pi^*_{(MCPO)}$
			283A→293A	–0.28207	
			275B→298B	0.24635	
			276B→296B	–0.26077	
			277B→286B	0.28416	
13	409	0.0000	280A→303A	–0.41025	$\pi_{(MCPO)}$-
			272B→287B	0.31541	$\pi^*_{(MCPO)}$
			274B→297B	0.41173	
14	409	0.0000	279A→293A	–0.26371	$\pi_{(MCPO)}$-
			281A→302A	0.30087	$\pi^*_{(MCPO)}$
			273B→286B	0.26670	

Table S7. Atomic orbital contribution to MOs appearing in the main configuration of the (a) first and (b) second lowest π-4f CT excited state of **Eu-MCPO** in THF solvent using the optimized structure (9th and 11th excited state in Table S6). There is very small mixing of the π orbitals of MCPO and the 4f orbital of Eu.

MO	4f	MCPO-1	MCPO-2	NO_3
289A	0.00011	0.00007	0.99621	0.00310
290A	0.00054	0.00058	0.99250	0.00512
292A	0.95651	0.00374	0.00467	0.03292

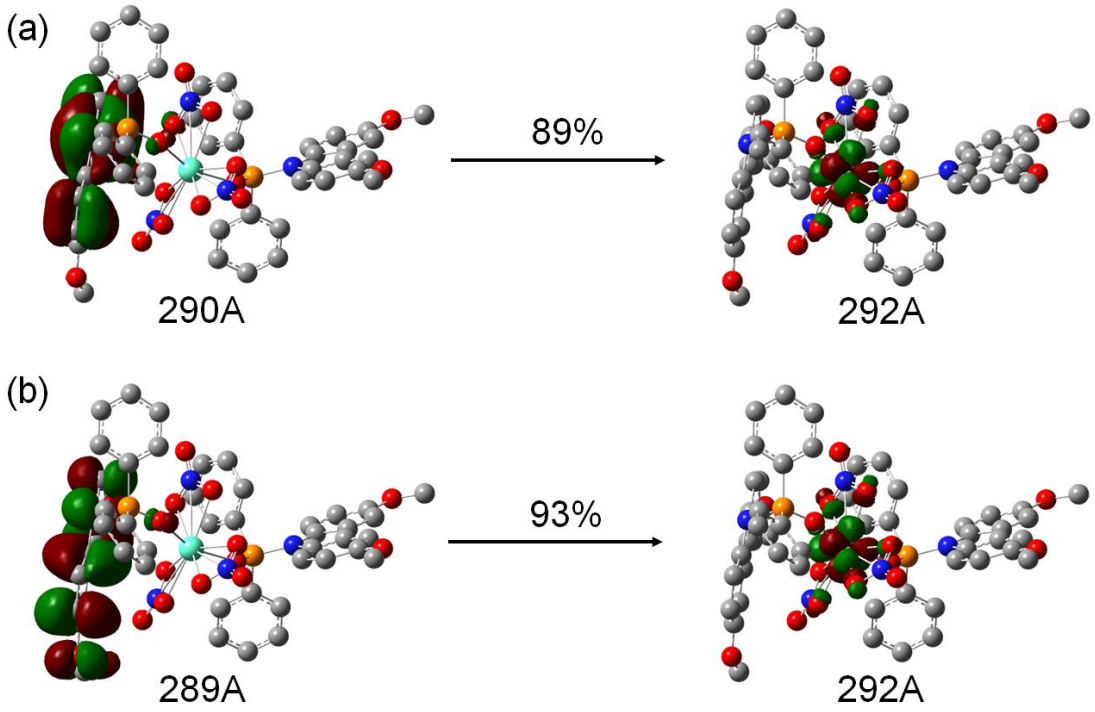

Figure S13. Transition orbital analysis of the (a) first and (b) second lowest π-4f CT excited state of **Eu-MCPO** in THF solvent using the optimized structure (9th and 11th excited state in Table S6).

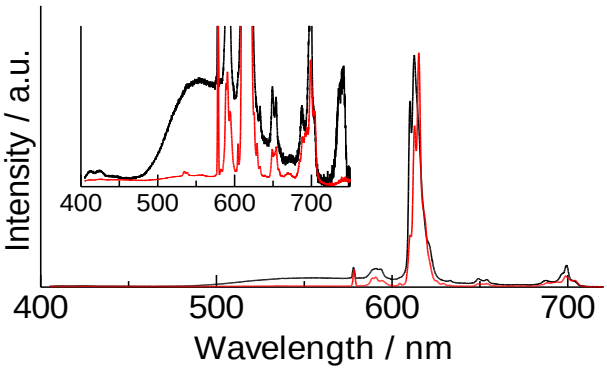

Figure S14. Emission spectra of **Eu-MCPO** in solid states at 300 K (black line) and 100 K (red line) under degassed condition. λ_{ex} = 368 nm.

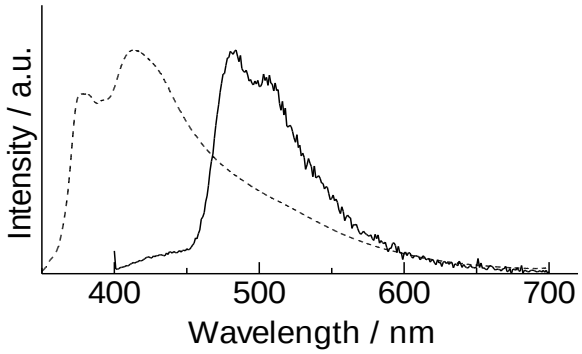

Figure S15. Emission spectra of MCPO in 2Me-THF at 100 K (broken line, 0.1 mM, λ_{ex} = 325 nm) and **Gd-MCPO** in solid states at 100 K (solid line, λ_{ex} = 330 nm, 20 msec delay). Normalized by intensity maxima.

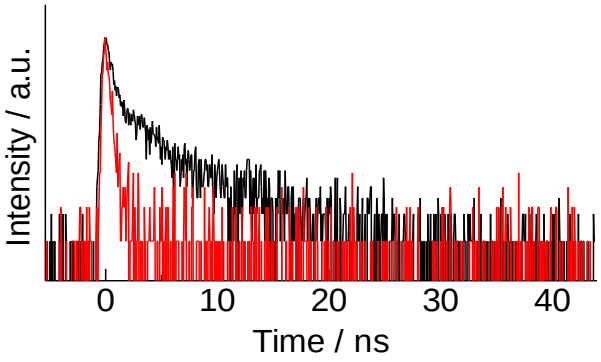

Figure S16. Emission decay of **Eu-MCPO** in solid states at 100 K under degassed condition (black line, λ_{ex} = 368 nm, λ_{em} = 570 nm). Prompt (red line).

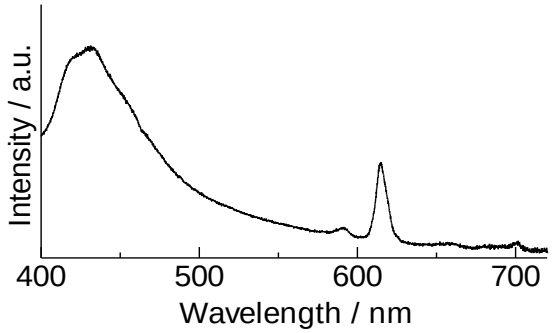

Figure S17. Emission spectrum of **Eu-MCPO-H_2O** in solid state at 300 K under degassed condition (λ_{ex} = 330 nm).

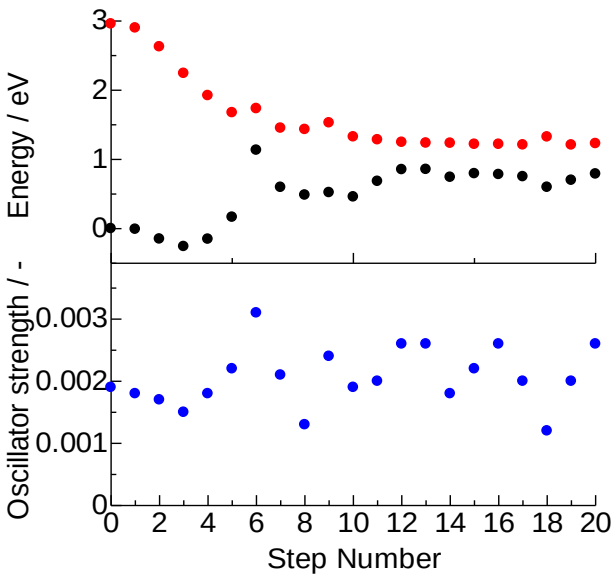

Figure S18. Structural relaxation of **Eu-MCPO** on the π-4f CT excited state in vacuum condition was approximately evaluated by excited-state optimization using TDDFT calculations. Changes of the π-4f CT-excited-state energies (red), ground-state energies (black), and oscillator strengths (blue) for first 20 steps during the optimization process on the lowest π-4f CT excited state (9th excited state in Table S2) were shown.

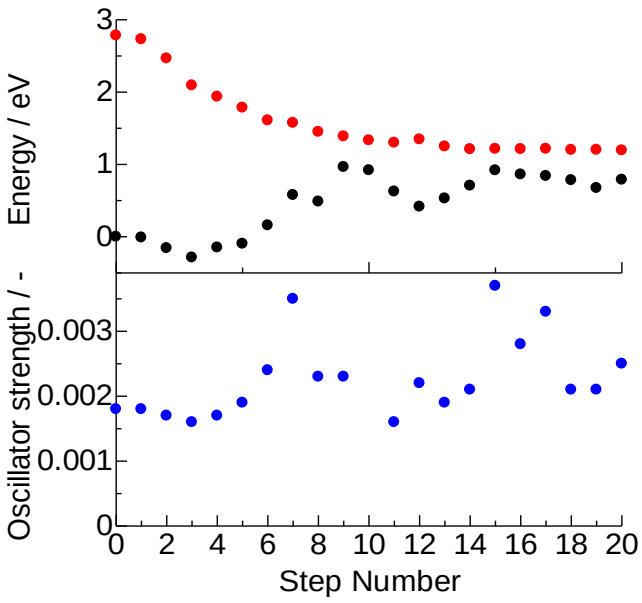

Figure S19. Structural relaxation of **Eu-MCPO** on the π-4f CT excited state in THF solvent was approximately evaluated by excited state optimization using TDDFT calculations with PCM method. Changes of the π-4f CT excited state energies (red), ground state energies (black), and oscillator strengths (blue) for first 20 steps during the optimization process on the lowest π-4f CT excited state (9th excited state in Table S6) were shown.

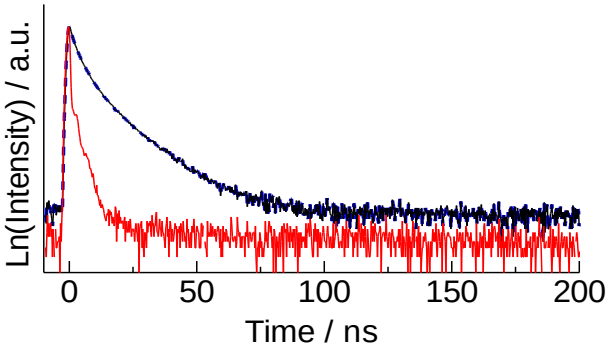

Figure S20. Emission decay of **Eu-MCPO** in $CHCl_3$ at 300 K (black line, λ_{ex} = 375 nm, λ_{em} = 570 nm). Prompt (red line). Fitting curve assuming a double exponential decay (blue dashed line).

S4. Emission analyses of Eu-MCPO in the 2Me-THF condition

The emission spectra of **Eu-MCPO** at 100 and 300 K excited by the LMCT bands are shown in Figure S21. At low temperatures, a broad emission band at approximately 530 nm, as well as sharp 4f-4f emission bands at 579, 590, 610, 650, and 700 nm, were observed for **Eu-MCPO**. The broad emission band was considered to originate from the π-f charge-transfer excited states. The 4f-4f emission band decreased with increasing temperature, indicating that an energy transfer pathway between the $^5D_0$ and π-4f CT excited states was present.

To confirm the energy transfer pathway, time-resolved emission spectra of **Eu-MCPO** in 2Me-THF (10 mM) at 300 K were estimated using the π-4f CT excitation (λ_{ex} = 440 nm, Figure S22). A weak broad emission band at an upper baseline of approximately 560 nm—attributed to π-4f CT and the sharp emission band at 620 nm assigned to $^5D_0 \rightarrow {}^7F_2$ were observed at 0–10 ns and 95–105 μs after excitation, respectively. These results suggest that an energy transfer pathway from the π-4f CT excited state to $^5D_0$ was present. This photophysical behavior was also observed at 100 K (Figure S23). The emission decay curve for the π-4f CT emission band (λ_{em} = 570 nm) at 300 K is shown in Figure S24. The **Eu-MCPO** in 2Me-THF exhibited a nanosecond-scale lifetime similar to that observed in the $CHCl_3$ condition; however, determining the precise emission lifetime was difficult because of the strong overlapping IRF curve. Time-resolved emission spectra were also obtained using optical excitation at 400 nm, which was based on the

dual transition from the ground state to the MCPO S_1 and π-4f CT states (Figure 2). Immediately after excitation, a broad emission was observed at approximately 440 nm (Figure S25a). This emission band mainly originated from the fluorescence of the MCPO ligand moiety (Figure S15). The emission bands at 535, 555, and 583 nm, which were observed within the hundreds-of-nanoseconds time frame (Figure S25b), were assigned to the transitions of $^5D_1 \rightarrow {}^7F_1$, $^5D_1 \rightarrow {}^7F_2$, and $^5D_1 \rightarrow {}^7F_3$, respectively.[S13] The bands at 590 and 615 had the longest lifetime (Figure S25c) and were assigned to $^5D_0 \rightarrow {}^7F_1$ and $^5D_0 \rightarrow {}^7F_2$, respectively. These results indicated that $^5D_0 \rightarrow {}^7F_J$ emission by ligand excitation occurred *via* energy transfer from the MCPO T_1 state to the $^5D_1$ state.

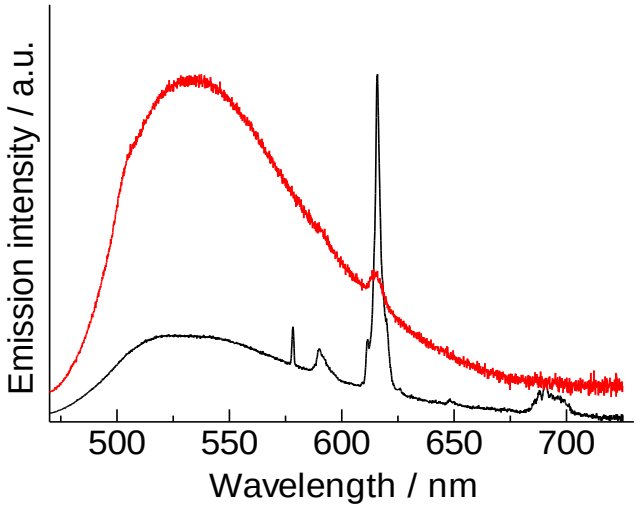

Figure S21. Emission spectra of **Eu-MCPO** in 2Me-THF at 300 K (black line, λ_{ex} = 440 nm) and 100 K (red line, λ_{ex} = 440 nm). Normalized by intensity maxima.

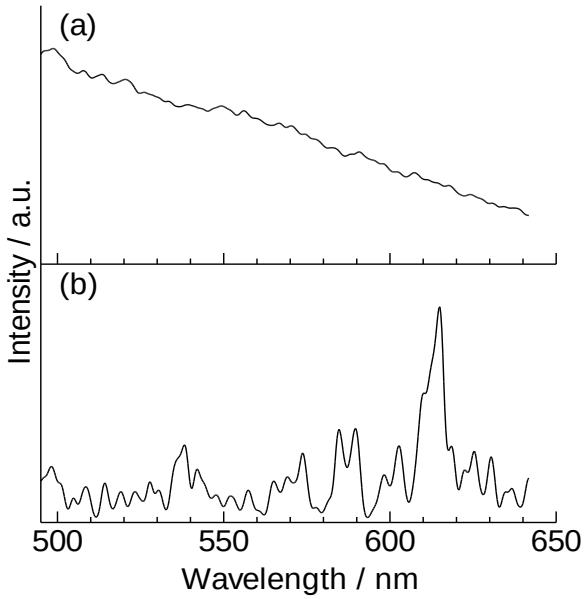

Figure S22. Time-resolved emission spectra of **Eu-MCPO** in 2Me-THF (10 mM) at 300 K excited by 440 nm. Emission spectra were obtained from the streak images by the time integration of (a) 0–10 ns and (b) 95–105 μs.

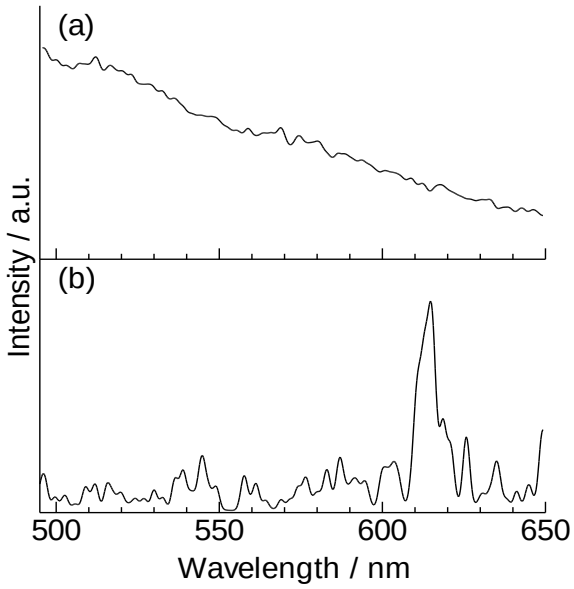

Figure S23. Time-resolved emission spectra of **Eu-MCPO** in 2Me-THF (10 mM) at 100 K excited by 440 nm. Emission spectra were obtained from the streak images by the time integration of (a) 0–10 ns and (b) 95–105 μs.

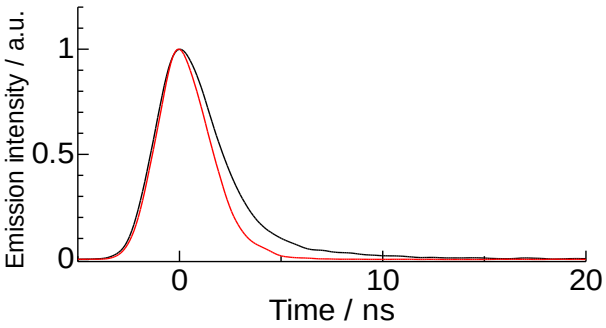

Figure S24. Emission decay curves of **Eu-MCPO** in 2Me-THF (10 mM) at 570 nm (black line) and instrumental response function (red line).

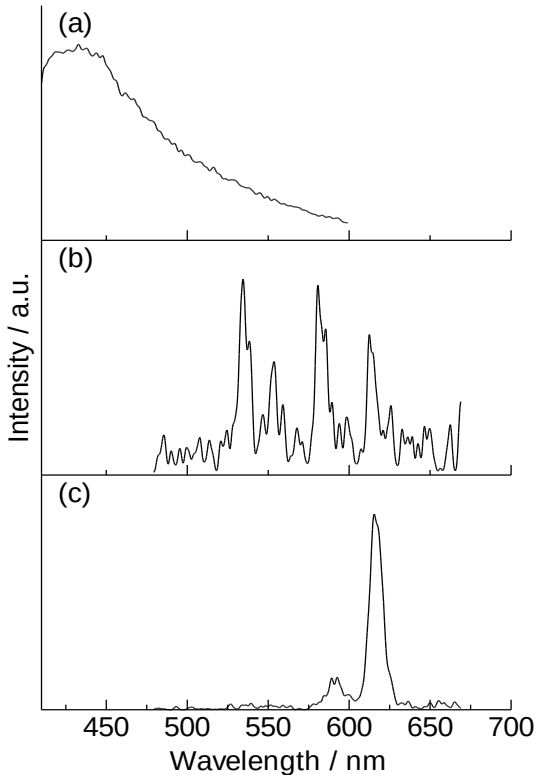

Figure S25. Time-resolved emission spectra of **Eu-MCPO** in 2Me-THF (10 mM) at 300 K excited by 400 nm. Normalized emission intensity spectra were obtained from the streak images by the time integration of (a) 0–1 ns, (b) 195–205 ns, and (c) 14.5–15.5 μs.

References

S1. Frisch, M. J., Trucks, G. W., Schlegel, H. B., Scuseria, G. E., Robb, M. A., Cheeseman, J. R., Scalmani, G., Barone, V., Petersson, G. A., Nakatsuji, H., Li, X., Caricato, M., Marenich, A. V., Bloino, J., Janesko, B. G., Gomperts, R., Mennucci, B., Hratchian, H. P., Ortiz, J. V., Izmaylov, A. F., Sonnenberg, J. L., Williams-Young, D., Ding, F., Lipparini, F., Egidi, F., Goings, J., Peng, B., Petrone, A., Henderson, T., Ranasinghe, D., Zakrzewski, V. G., Gao, J., Rega, N., Zheng, G., Liang, W., Hada, M., Ehara, M., Toyota, K., Fukuda, R., Hasegawa, J., Ishida, M., Nakajima, T., Honda, Y., Kitao, O., Nakai, H., Vreven, T., Throssell, K., Montgomery, J. A., Jr., Peralta, J. E., Ogliaro, F., Bearpark, M. J., Heyd, J. J., Brothers, E. N., Kudin, K. N., Staroverov, V. N., Keith, T. A., Kobayashi, R., Normand, J.,

Raghavachari, K., Rendell, A. P., Burant, J. C., Iyengar, S. S., Tomasi, J., Cossi, M., Millam, J. M., Klene, M., Adamo, C., Cammi, R., Ochterski, J. W., Martin, R. L., Morokuma, K., Farkas, O., Foresman, J. B., Fox, D. J. Gaussian, Inc., Wallingford CT, **2016**.

S2. Becke A. D. Density-functional thermochemistry. III. The role of exact exchange. *J. Chem. Phys.* **1993**, 98, 5648–5652.

S3. Stephens, P. J., Devlin, F. J., Chabalowski, C. F., Frisch, M. J. Ab initio calculation of vibrational absorption and circular dichroism spectra using density functional force fields. *J. Phys. Chem.* **1994**, 98, 11623–11627.

S4. Grimme, S., Antony, J., Ehrlich, S., Krieg, H. A. Consistent and accurate Ab initio parametrization of density functional dispersion correction (DFT-D) for the 94 elements H-Pu cite. *J. Chem. Phys.* **2010**, 132, 154104.

S5. Becke, A. D. Density-functional exchange-energy approximation with correct asymptotic behavior. *Phys. Rev. A* **1988**, 38, 3098–3100.

S6. Lee, C., Yang, W., Parr, R. G. Development of the colle-salvetti correlation-energy formula into a functional of the electron density. *Phys. Rev. B* **1988**, 37, 785–789.

S7. Tawada, Y., Tsuneda, T., Yanagisawa, S., Yanai, T., Hirao, K. A Long-range-corrected time-dependent density functional *J. Chem. Phys.* **2004**, 120, 8425–8433.

S8. Dolg, M., Stoll, H., Savin, A., Preuss, H. Energy-adjusted pseudopotentials for the rare earth elements. *Theor. Chim. Acta* **1989**, 75, 173–194.

S9. Dunning, T. H. Gaussian basis sets for use in correlated molecular calculations. I. The atoms boron through neon and hydrogen. *J. Chem. Phys.* **1989**, 90, 1007–1023.

S10. Woon, D. E., Dunning, T. H. Gaussian basis sets for use in correlated molecular calculations. III. The atoms aluminum through Argon. *J. Chem. Phys.* **1993**, 98, 1358–1371.

S11. Tomasi, J., Mennucci, B., Cammi, R. Quantum mechanical continuum solvation models. *Chem. Rev.* **2005**, 105, 2999–3093.

S12. O'Boyle, N. M., Tenderholt, A. L., Langner, K. M. cclib: A library for package-independent computational chemistry algorithms. *J. Comp. Chem.* **2008**, 29, 839–845.

S13. Ma, C.-G., Brik, M. G., Liu, D.-X., Feng, B., Tian, Y., Suchocki, A. Energy level schemes of f^N electronic configurations for the di-, tri-, and tetravalent lanthanides and actinides in a free state. *J. Lumin.* **2016**, 170, 369–374.